LANGMUIR

pubs.acs.org/Langmuir Article

Role of Interfacial Tension on Viscous Multiphase Flows in Coaxial Microfluidic Channels

Thai Dinh and Thomas Cubaud*

Cite This: *Langmuir* 2021, 37, 7420–7429 Read Online

ACCESS | Metrics & More | Article Recommendations

ABSTRACT: We experimentally investigate the influence of interfacial tension on liquid/liquid microflows for fluids having large viscosity contrasts. A coaxial microdevice is employed to examine the situation where a less-viscous fluid is injected in a sheath of a more-viscous fluid using both immiscible and miscible fluid pairs. Data obtained from high-speed imaging reveal a variety of regular flow regimes, including dripping, jetting, wavy, core-annular, diffusive jet, mist, and inverted thread flow patterns. Flow maps are delineated over a wide range of injection flow rates, and an original methodology based on periodic pattern analysis is developed to clarify relationships between interfacial dynamics and fluid properties of multiphase materials. Specifically, we show the smooth evolution of droplet size and spacing at the transition between dripping and jetting flows and develop scaling relationships based on capillary numbers to predict droplet flow morphologies. For similar flow conditions, reducing interfacial tension leads to a significant decrease in droplet size. For miscible fluid pairs, diffusive jets are observed at low Péclet numbers, whereas wavy core-annular flows are obtained at moderate Reynolds numbers for both immiscible and miscible fluids. This work provides a unifying description of the influence of interfacial properties on viscous microflow phenomena.

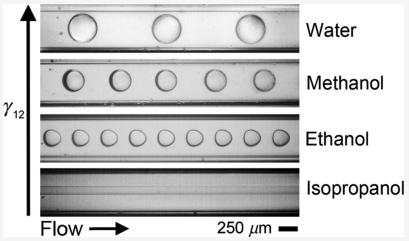

1. INTRODUCTION

Interfacial tension is of great importance in numerous industrial and natural processes, including emulsification[1] and oil recovery,[2] and plays a fundamental role in the stability of colloidal systems.[3] Capillary forces have long been recognized as dominant in determining the forms of cells as well as many biological growth processes.[4] In liquid–liquid dispersions, interfacial tension strongly affects the shape of the fluid interface and controls the size of droplets between immiscible fluids. By contrast, the transition layer between miscible fluids is diffusive and transient,[5] and the interfacial region widens instead of contracting due to negligible interfacial tension. In the presence of external flows, however, interfacial deformations between miscible fluids streams can resemble those of immiscible streams due to the predominance of viscous and inertial stresses[6] and a few studies have examined fluid phenomena with ultralow interfacial tension.[7−10] In addition, hydrodynamic methods have shown the possibility to control the dimension of droplets or bubbles across a variety of multiphase flow regimes.[11] Therefore, size distribution and arrangement of multifluid materials depend on a subtle combination of fluid properties and flow conditions and better characterizing the individual contribution of interfacial tension to multiphase flow morphologies would advance general understanding as well as improve capabilities for the synthesis of advanced fluid materials.

Microfluidic systems enable enhanced flow manipulations with precise control of microgeometries over a wide range of flow rates. Droplets and bubbles can be produced one-by-one for the generation of monodisperse emulsions and foams in the presence of a surfactant.[12−17] Typical microflow geometries used for the generation of droplets include T-junctions,[18−20] focusing sections,[21−23] and coaxial channels.[24−27] Coaxial microchannels are composed of small centerline injectors inserted in ducts of various sizes and offer versatility and high throughput for an array of applications, including synthesis of nanoparticles[28−30] and microfibers.[31−33] Hence, microfluidic injectors are practical flow devices that allow for manipulating a wide range of materials. The role of basic fluid properties in the interaction and combination of fluid streams in coaxial microchannels, however, has remained relatively unexplored despite their potential for methodical examination of novel multiphase flow configurations with immiscible and miscible fluids at the small scale.

Here, we systematically investigate the role of interfacial tension on the microfluidic formation of droplets and jets in the presence of large viscosity contrasts in coaxial microfluidic devices. We conduct a comprehensive study of microflow phenomena with fluid pairs having various interfacial tensions at a constant viscosity ratio to determine the influence of fluid

Received: March 19, 2021
Revised: May 30, 2021
Published: June 11, 2021

https://doi.org/10.1021/acs.langmuir.1c00782
Langmuir 2021, 37, 7420–7429

interfacial properties on regime boundaries and morphological transitions of segmented and continuous flows. We previously employed square hydrodynamic focusing junctions to examine the microflow behavior of immiscible fluids having low interfacial tension[34] and the phenomenon of viscous thread swelling with miscible fluids.[35] In the current investigation, coaxial microdevices are utilized to probe and compare microflow regimes having negligible interfacial tension using miscible fluids and microflow patterns from low-to-large interfacial tension using immiscible fluids. We first investigate the location of multiphase patterns on broad flow maps and discuss the classification of dispersed and separated flows. A periodic pattern analysis of dripping and jetting flows is then implemented with focus on the evolution of droplet size and spacing as a function of interfacial tension and flow parameters. This study subsequently centers on separated flow characteristics with focus on the evolution of the envelope amplitude of various streams and the stable jet length. The wavelength, frequency, and celerity of capillary and inertial waves developing along the central core are also examined, and intriguing flow regimes, such as mist flow and inverted thread regimes, are reported at a large flow velocity. This work provides a quantitative comparative analysis of the flow behavior of immiscible and miscible fluids across a broad range of fluid properties and flow parameters.

2. EXPERIMENTAL METHODS

Coaxial microchannels are made of an assembly of square capillary tubes having internal width h = 500 μm and microneedles of tip diameters b = 40 ± 5 μm (Figure 1a). Microneedles are fabricated

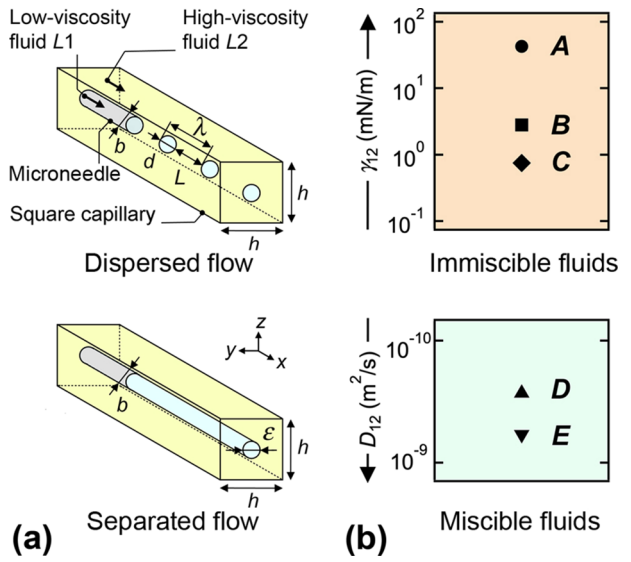

Figure 1. (a) Schematics of coaxial microchannels with main features of dispersed and separated flows, including droplet diameter d and spacing L as well as spatial period λ and stable jet diameter ε. (b) Variation of interfacial tension γ_{12} between immiscible fluid pairs A, B, and C and diffusion coefficient D_{12} for miscible fluid pairs D and E.

using a micropipette puller with circular borosilicate glass tubes of an outer diameter of 500 μm. The puller parameters are adjusted to create long tapered needles with parallel walls, which are sometimes referred to as aspiration pipettes. These microneedles have small outlet diameters b and are subsequently inserted into square capillary tubes. As the large outer diameter of a needle inlet matches the internal width of a square capillary, the small needle outlet is readily aligned with the capillary central axis to form a miniaturized version of a centerline injector. The microneedle inlet is then connected to a syringe pump to inject a low-viscosity fluid L1 having dynamic viscosity η_1 at volumetric flow rate Q_1, and the inlet of the square capillary is connected to another syringe pump to simultaneously introduce a high-viscosity fluid L2 having viscosity η_2 at flow rate Q_2 into the device. To visualize flows, a high-speed camera equipped with a macro lens and an extension tube is placed above the microfluidic device and experimental micrographs are analyzed using image-processing routines.

Fluid pairs are selected to investigate the role of interfacial tension γ_{12} and diffusion coefficient D_{12} on microfluidic flow patterns and transitions at a fixed viscosity ratio $\chi = \eta_1/\eta_2 \approx 10^{-2}$, as shown in Table 1. For the external fluid L2, silicone oils are typically blended

Table 1. Properties of Fluid Pairs Used with a Fixed Viscosity Ratio $\chi = \eta_1/\eta_2 \approx 10^{-2}$ and Varying Interfacial Tension γ_{12} and Diffusion Coefficient D_{12}

Fluid pair	L1	η_1 (cP)	L2	η_2 (cP)	γ_{12} (mN m^{-1})	D_{12} (m^2 s^{-1})
A	Water	1.0	Oil	97	42.7	
B	Methanol	0.58	Oil	56	2.8	
C	Ethanol	1.32	Oil	128	0.75	
D	Isopropanol	2.10	Oil	203		2.7×10^{-10}
E	Oil	1.0	Oil	97		5.9×10^{-10}

with a reference oil having η_2 = 97 cP according to the manufacturer's guidelines to obtain the desired viscosity, which is then measured for accuracy using tube viscometers. The viscosity of the inner fluid L1 is also tested, and values of interfacial tension γ_{12} and diffusion coefficient D_{12} for each fluid pair are similar to previous work using the same oil and alcohol from manufacturers.[34,35] Overall, the use of water, methanol, and ethanol for $L1$ enables wide variations of γ_{12} for the immiscible fluid pairs A to C and employing isopropanol and silicone oil for the center fluid allows for the formation of partially and fully miscible fluid pairs D and E (Figure 1b).

Depending on fluid properties and flow parameters, a variety of dispersed and separated flow patterns are experimentally observed. In the dispersed flow regime, discrete droplets are formed from fluid L1 and transported along the channel in the continuous phase L2. Parameters of interest include the droplet length d and spacing L along the flow direction (Figure 1a—top). These two simple quantities are useful to interrogate the combined influence of flow rates, Q_1 and Q_2, and interfacial tension γ_{12} on multiphase flows across various fluid pairs. Compound quantities, such as the aspect ratio d/L and wavelength $\lambda = d + L$ of segmented flows, are also practical to characterize the role of fluid and flow properties and permit quantitative comparison with wavy separated flows. In general, separated flows are obtained when fluids form distinct or blurry continuous streams. An important parameter in this case is the central stream diameter of core-annular flows or stable jets ε (Figure 1a—bottom). Useful dimensionless numbers include the capillary number $Ca = \eta_2 V/\gamma_{12}$, which compares viscous and capillary stresses, for immiscible fluids and the Péclet number $Pe = hV/D_{12}$, which compares advection and diffusion, for miscible fluids. The Reynolds number $Re = \rho_1 Vh/\eta_1$ quantifies the relative importance of inertial and viscous stresses and finds use in the description of wave regimes. The characteristic velocity V typically corresponds to the average superficial velocity $(Q_1 + Q_2)/h^2$ for droplet and wave flows or the interfacial velocity $2Q_2/h^2$ for diffusive separated flows. Overall, devices are operated for capillary numbers Ca ranging between 10^{-6} and 10^{-1} for immiscible fluids and for Péclet numbers varying between 10^2 and 10^5 for miscible fluids. Variations of Reynold number Re span between 10^{-2} and 10^1. In this work, we show that while introducing a dichotomy between dispersed and separated flows provides a useful classification, numerous microflow patterns adopt intermediate features.

https://doi.org/10.1021/acs.langmuir.1c00782
Langmuir 2021, 37, 7420−7429

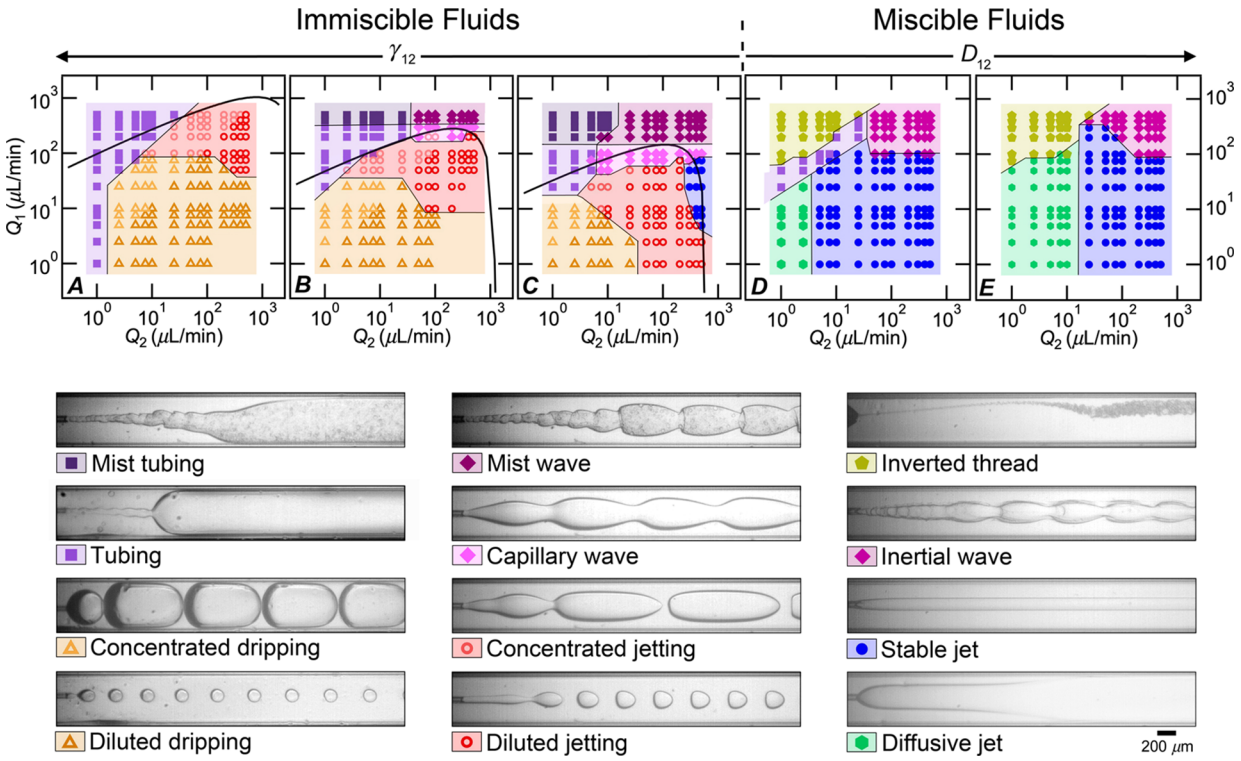

Figure 2. Top: Flow maps of each fluid pair A, B, C, D, and E based on injection flow rates Q_1 and Q_2. The solid curve corresponds to prediction for dispersed/separated flow transition. Bottom: Experimental micrographs of basic flow regimes, including dripping, jetting, stable and diffusive jet, capillary and inertial wave, tubing, inverted thread, and mist flow patterns.

3. RESULTS AND DISCUSSION

3.1. Flow Maps. A broad variety of flow regimes are observed for the five fluid pairs investigated (Figure 2). To reveal the influence of fluid properties, flow maps are delineated based on flow rates of injection Q_1 and Q_2. While flow maps are typically presented in terms of velocities, such as superficial velocities $J_1 = Q_1/h^2$ and $J_2 = Q_2/h^2$, or dimensionless numbers, including capillary number Ca for immiscible fluids and Péclet number Pe for miscible fluids, here, the wide variation of velocity profiles in dispersed and separated flows at very low χ together with the presence of both diffusive and capillary flows suggests the use of flow rates as base parameters to facilitate comparison of flow regimes across fluid pairs. As the ratio of individual bulk properties remains constant, $\chi = \eta_1/\eta_2 \sim 10^{-2}$, for a similar geometry, $b/h \sim 10^{-1}$, this approach directly shows how mutual fluid properties, such as γ_{12} or D_{12}, affect the occurrence of specific flow regimes and transition. Previous work, conducted at fixed γ_{12} and various $\chi \ll 1$ in square microchannels,[34] proposed a simple analytical criterion based on droplet velocity and wave celerity for predicting the transition between dispersed and separated flows. Such transition curves are here reported as thick lines for the immiscible fluid pairs A, B, and C on Figure 2 and show good qualitative agreement with data.

Dispersed flows consist of dripping and jetting regimes. Dripping flows are found at a low total flow rate $Q_T = Q_1 + Q_2$ and are characterized by the regular emission of droplets near the fluid contactor. At larger flow rates, a jet protrudes from the microneedle and ruptures further downstream into jetting droplets. The transition between dripping and jetting flow is shifted toward larger values of Q_T as γ_{12} increases and corresponds to a more or less fixed capillary number Ca = $\eta_1 Q_T/(\gamma_{12} h^2) \sim 0.5$. In each regime, we define two subregimes, including diluted flows for $\varphi = Q_1/Q_2 < 1$ and concentrated flows for $\varphi > 1$. Given our small needle $b/h \sim 10^{-1}$, droplet size d and spacing L are uniformly distributed in diluted flows while polydispersity is typically observed in concentrated flows. Indeed, the central stream experiences a significant deceleration which favors droplet coalescence at the fluid junction for concentrated flows with large d and small L.

Separated flows comprise core-annular flows with three main regimes, including tubing, jet, and wave. At large $\varphi > 10$, tubing flows display a central stream that occupies the square channel width $\varepsilon \sim h$ while at lower φ, jet flows exhibit a uniform core diameter $\varepsilon < h$. Wave regimes are characterized by the presence of periodic undulations along the core with a spatially increasing wavelength λ for capillary waves at relatively low Q_T and a spatially decreasing λ for inertial waves at larger Q_T. For fluid pairs A, B, and C with non-negligible γ_{12}, mist flows made of tiny droplets of high-viscosity fluid L2 entrained in the core are observed at large Q_1 for both tubing and wave regimes. This pattern is often seen in heat-transfer applications.[36−38] By contrast, for fluid pairs D and E with $\gamma_{12} \sim 0$, an intriguing "inverted thread" regime is revealed at very large $\varphi > 10^2$. Such a flow consists of the phase inversion of a core-annular flow where a thread of the more-viscous fluid L2 becomes encapsulated by less-viscous liquid L1. The formation of a viscous thread convected in a low-viscosity fluid significantly reduces viscous dissipation and results from the complex hydrodynamic interplay between concentric and core-annular flows at the fluid junction. Another flow regime specific to miscible fluids is labeled diffusive jet and is observed at low Q_2 for fluid pairs D and E and corresponds to a jet progressively blending with the outer fluid in the field of view close to the fluid contactor. Distinction

https://doi.org/10.1021/acs.langmuir.1c00782
Langmuir 2021, 37, 7420−7429

between stable and diffusive jets is made through visual inspection of micrographs and occurs at a critical Q_2, which grows with diffusion coefficient D_{12}, and corresponds to a critical Péclet number $Pe = 2Q_2/(D_{12}h) \sim 1.2 \times 10^3$. Overall, flow map comparison between immiscible and miscible fluid pairs shows partial similarities for separated flows at large Q_T and significant disparities at low Q_T with the presence of droplet flows for immiscible fluids and diffusive flows for miscible fluids. Therefore, over the range of parameters investigated, we assume that $\gamma_{12} = 0$ for the miscible fluid pairs D and E, which form a control group in the study of the role of non-negligible γ_{12} on multiphase flows at very low $\chi \sim 10^{-2}$ using immiscible fluid pairs A, B, and C.

3.2. Dispersed Flows. *3.2.1. Droplet Size.* Microfluidic geometries provide an advantageous environment for the continuous generation of monodisperse droplets. In hydrodynamic focusing systems, the droplet size d typically increases with the volume fraction $\alpha_1 = Q_1/(Q_1 + Q_2)$, which leads to the formation of diluted flows with small d and large L for a low flow rate ratio $\varphi = Q_1/Q_2 < 1$ and concentrated flows with large d and small L for high $\varphi > 1$. Predicting d, however, remains challenging over a range of fluid properties, γ_{12}, η_1, and η_2, flow parameters, Q_1 and Q_2, and local geometry, h and b. Here, we employ the method of iso-φ curves to examine the evolutions of diluted flows over a wide range of γ_{12} in a coaxial device with $b/h \sim 10^{-1}$. In particular, we examine the evolution of d at fixed φ, *i.e.*, for fixed droplet concentration α_1, as a function of the total flow rate Q_T for fluid pairs A, B, and C (Figure 3a—top). For constant $\chi = \eta_1/\eta_2 = 10^{-2}$, two distinct behaviors are observed where d is independent of φ and decreases with Q_T for large γ_{12} (fluid pair A) and where d/h strongly depends on φ and increases with Q_T for small γ_{12} (fluid pair C). A somewhat intermediate behavior is observed for fluid pair B over the same range of Q_T. To account for the influence of γ_{12} on the evolution of d at a fixed concentration, all iso-φ curves of the three fluid pairs are combined and plotted against the capillary number $Ca_T = \eta_2 Q_T/(\gamma_{12}h^2)$ (Figure 3a—bottom). This unifying approach reveals the overall behavior of d across fluid pairs and flow regimes, including dripping droplets at low Ca_T and jetting droplets at larger Ca_T.

For the dripping regime, as iso-φ curves appear to progressively separate from a limiting curve associated with very small concentrations, we plot d/h as a function of Ca_T for all dripping droplets with $\varphi \leq 0.25$ in Figure 3b. Data show good agreement with an expression of the form $d/h = 0.15Ca_T^{-1/3}$, which provides a simple estimate of the size of highly diluted droplets having a spherical shape at low Ca_T with fine control of d/h between 1 and $b/h \sim 10^{-1}$, given our small injection needle.

In the jetting regime, Q_T affects droplet morphology and low-viscosity droplets appear significantly deformed due to the relative large influence of viscous stresses associated with the continuous phase at high $Ca_T > 1$. In this situation, d/h depends primarily on the flow rate ratio φ instead of Ca_T and data are well-fitted with a scaling of the type $d/h = 0.8\varphi^{1/3}$ (Figure 3c).

3.2.2. Droplet Spacing. Another important characteristic of dispersed flows is the spacing between droplets L. To analyze the evolution of L, we develop an approach similar to that of d and examine the shape of iso-φ curves as a function of Q_T in diluted dripping and jetting regimes (Figure 4a—top). A somewhat opposite trend to d is observed with L-curves

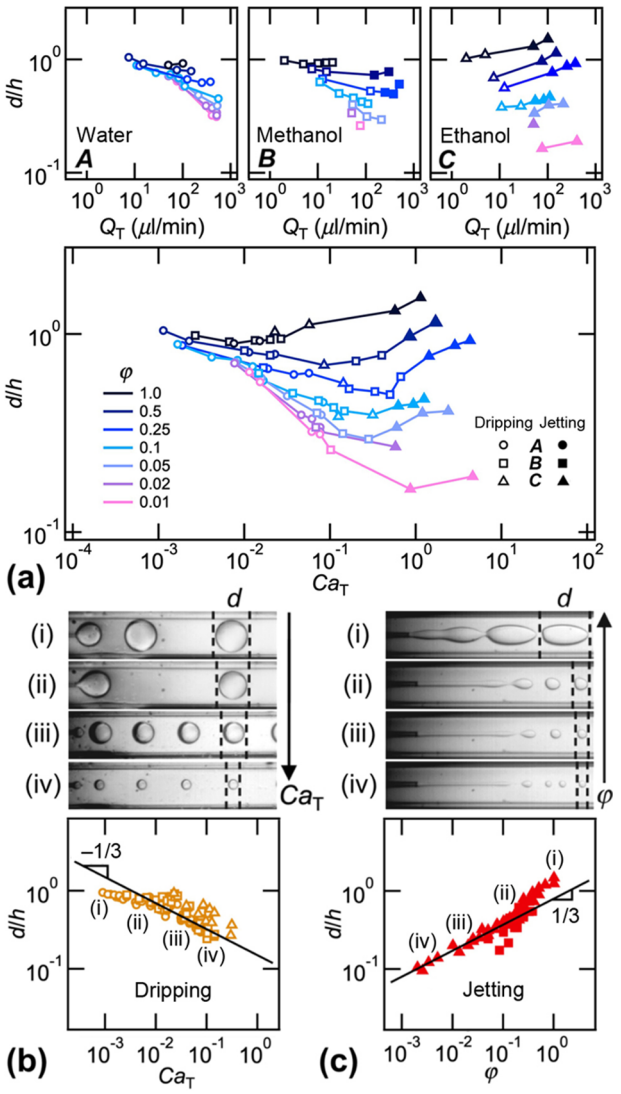

Figure 3. Diluted droplet size d/h across flow regimes and fluid pairs. Open symbols correspond to dripping and solid symbols correspond to jetting with fluid pairs A (○, ●), B (□, ■), and C (△,▲). (a) Top: Evolution of d/h along iso-φ curves as a function of Q_T for immiscible fluid pairs. Bottom: Combined evolution of d/h at fixed φ *versus* Ca_T. (b) Top: Micrographs of dripping droplets with flow rates (Q_1, Q_2) in μL/min; fluid pair A: (i) (2.5, 10) and (ii) (2.5, 25); fluid pair B: (iii) (5, 25) and (iv) (1, 75). Bottom: droplet size d/h *versus* Ca_T for $\varphi \leq 0.25$, solid line: $d/h = 0.15Ca_T^{-1/3}$. (c) Top: Micrograph of jetting droplets; fluid pair C: (i) (50, 75), (ii) (5, 100), (iii) (2.5, 100), and (iv) (1, 100). Bottom: d/h as a function of φ. Solid line: $d/h = 0.8\varphi^{1/3}$.

strongly dependent on φ at large γ_{12} (fluid pair A) and independent of φ at small γ_{12} (fluid pair C). In all cases, the evolution of L at a constant ratio φ shows a monotonic decrease with flow rate Q_T. The combined evolution of L across fluid pairs is shown as a function of the capillary number Ca_T for various φ in Figure 4a—bottom. As indicated, iso-φ curves of L appear to follow a scaling of the form $L/h \sim Ca_T^{-1/3}$ for large Ca_T and $L/h \sim kCa_T^{-1/3}$ where the prefactor k is a function of φ for low Ca_T. In Figure 4b inset, we show that the coefficient k essentially follows the expression $k = 0.04\varphi^{-1}$, which suggests that L/h is a function of $1/(\varphi Ca_T^{1/3})$ for diluted dripping droplets. Overall, good agreement is found between data and the scaling $L/h = 0.05/(\varphi Ca_T^{1/3})$, although

https://doi.org/10.1021/acs.langmuir.1c00782
Langmuir 2021, 37, 7420−7429

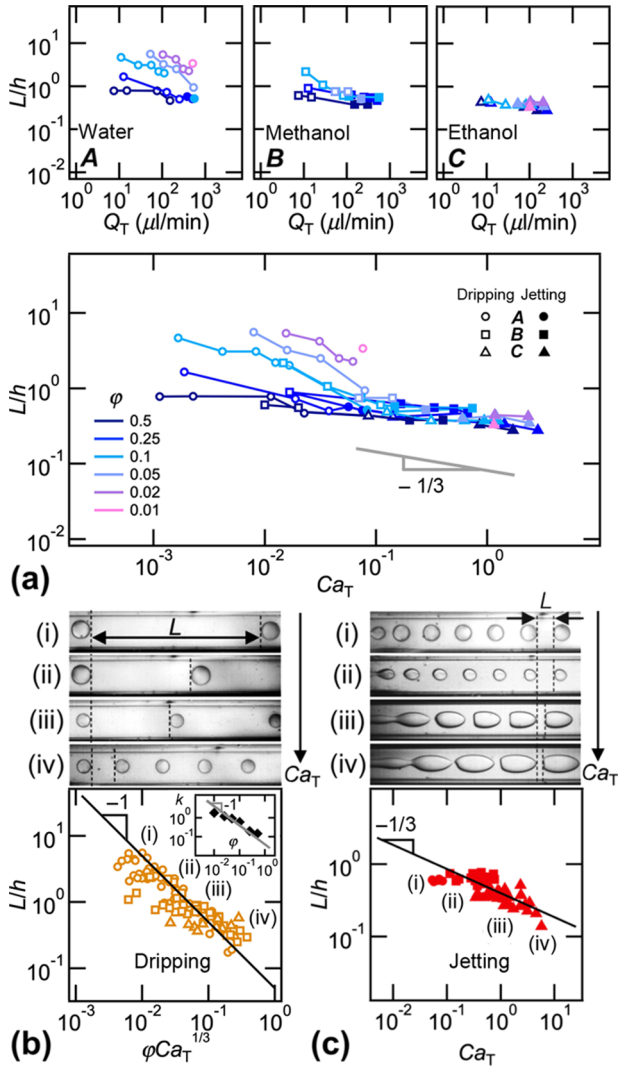

Figure 4. Diluted droplet spacing L/h across flow regimes and fluid pairs. Open symbols correspond to dripping and solid symbols correspond to jetting with fluid pairs A (○, ●), B (□, ■), and C (△,▲).(a) Top: Evolution of L/h along iso-φ curves as a function of Q_T for immiscible fluid pairs. Bottom: Combined evolution of L/h at fixed φ *versus* Ca_T. (b) Top: Micrographs of dripping droplets with flow rates (Q_1, Q_2) in μL/min, (i) fluid pair A (2.5, 100), (ii) (5, 100), (iii) (7.5, 300), and (iv) (25, 400). Bottom: droplet spacing L/h *versus* $\varphi Ca_T^{1/3}$ for $\varphi \leq 0.25$, solid line: $Lh = 0.05\varphi^{-1}Ca_T^{-1/3}$. Inset: Coefficient k *versus* φ. Solid line: $k = 0.04\varphi^{-1}$ (c) Top: Micrograph of jetting droplets, (i) fluid pair A (50, 300), (ii) fluid pair B (50, 300) and (iii) fluid pair C (25, 75) and (iv) (50, 100). Bottom: L/h as a function of Ca_T. Solid line: $d/h = 0.4Ca_T^{-1/3}$.

scattered data points are found below the curve for highly diluted cases (Figure 4b). Deviation to previous scaling is indeed expected for the case of very small droplets d, which display lower L since a relatively non-negligible amount of L2 is distributed between channel walls and droplets, thereby reducing the interdroplet distance over a spatial period of flow pattern. This aspect highlights the strong correlation between d and L and shows the limitation of independently analyzing droplet size and spacing. Such an approach is nonetheless useful for examining the overall behavior of dispersed flows. In the case of diluted jetting droplets shown in Figure 4c, better agreement is found between data and the scaling, $L/h = 0.4Ca_T^{-1/3}$, which is solely based on the capillary number.

3.2.3. Wavelength and Aspect Ratio. We now turn our attention to the behavior of segmented flows and examine the evolution of compound quantities, such as aspect ratio d/L and wavelength $\lambda = d + L$ of dispersed flows. Scaling laws of individual quantities d and L are useful for the development of functional relationships to quantify the morphology and dynamics of dripping and jetting flows. The wavelength λ describes the spatial periodicity of droplet patterns. Previous analysis shows that in a diluted dripping regime, $d/h = 0.15Ca_T^{-1/3}$ and $L/h \sim 0.05/(\varphi Ca_T^{1/3})$. Therefore, the normalized wavelength in the diluted dripping regime can be expressed as $\lambda/h \sim 0.05(2 + 1/\alpha_1)Ca_T^{-1/3}$ since $\alpha_1^{-1} = 1 + \varphi^{-1}$. This approach suggests that the quantity $(\lambda/h)Ca_T^{1/3}$ is a function of the droplet concentration α_1. While this work primarily focuses on the diluted regime, a nonmonotonic evolution of λ is observed, with large wavelengths found in both highly concentrated, $\alpha_1 \sim 1$, and highly diluted, $\alpha_1 \sim 0$, regimes with the presence of a minimal λ at $\alpha_1 \sim 0.5$ (Figure 5a). This behavior presents similarities with the evolution of

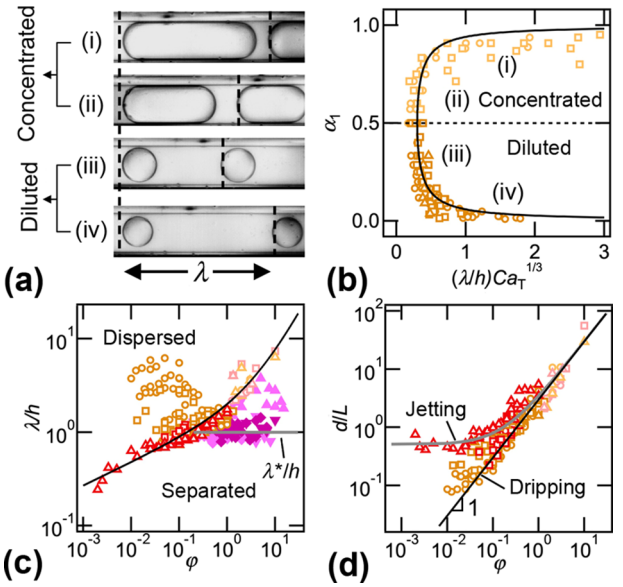

Figure 5. Evolution of compound quantities, wavelength $\lambda = d + L$ and aspect ratio d/L, of segmented flows. (a) Experimental micrographs of dispersed flows, fluid pair A, flow rates (Q_1, Q_2) in μL/min: (i) (2.5, 25), (ii) (2.5, 10), (iii) (2.5, 2.5), and (iv) (10, 2.5). (b) Relationship between wavelength and concentration of dripping flows, volume fraction α_1 as a function of $(\lambda/h)Ca_T^{1/3}$. Solid line: $(\lambda/h)Ca_T^{1/3} = 0.05(2 + 1/(1 - \alpha_1) + 1/\alpha_1)$. (c) Evolution of wavelength λ/h as a function of φ. Solid line: $\lambda/h = 1.5(\varphi^{1/4} + \varphi/3)$. (d) Aspect ratio d/L *versus* φ. Solid lines: $d/L = 3\varphi$ (dripping) and $d/L = 0.5 + 3\varphi$ (jetting).

dripping flows formed in hydrodynamic focusing sections[34] at low $\chi \ll 1$ where a symmetrical behavior is found between d and L for diluted and concentrated regimes. Therefore, we use an expression of the form $(\lambda/h)Ca_T^{1/3} = f(\alpha_1)$ where $f(\alpha_1) = 2 + 1/\alpha_1 + 1/(1 - \alpha_1)$ to describe the evolution of wavelength across the full range of droplet concentration α_1 in Figure 5b. Data scattering is observed for concentrated dripping flows due to overall polydispersity encountered with our reference geometry $b/h \sim 10^{-1}$ at large α_1.

The evolution of the wavelength λ in jetting flows significantly differs from that in dripping flows. In this situation, droplets result from the breakup deformation of

https://doi.org/10.1021/acs.langmuir.1c00782
Langmuir 2021, 37, 7420−7429

the low-viscosity thread formed at the central injection needle. As perturbations are convected with the flow, the most unstable wavelength is expected to remain independent of velocity, *i.e.*, the capillary number Ca_T, and should primarily depend on thread size ε and viscosity contrast χ, similar to the case of a static thread described by Tomotika's theory.[39] In this approach, the mode of the maximum instability $x = \pi\varepsilon/\lambda$, where ε is the diameter of the thread, is a function of the viscosity contrast χ. In our experimental inquiry, this argument leads to $\lambda \sim \varepsilon$ for fluid pairs A, B, and C, all having $\chi \sim 10^{-2}$. For such low χ, the central stream diameter ε is expected to scale as $\varepsilon \sim \varphi^{1/4}$, which yields a wavelength evolution with the flow rate ratio according to $\varepsilon \sim \varphi^{1/4}$. In Figure 5c, we represent the observed jetting wavelength together with λ of other regimes, including dripping and wave, as a function of flow rate ratio φ. The curve delineated by the jetting regime provides a reference for the boundary between dispersed and separated flows. Since at large φ, previous work showed that $\lambda/h \sim d/h \sim \varphi$, we expect $\lambda \sim \varphi$ for $\varphi \gg 1$ and $\lambda \sim \varphi^{1/4}$ for $\varphi \ll 1$; therefore, we curve-fit jetting data with the expression $\lambda/h = 1.5(\varphi^{1/4} + \varphi/3)$ and find good qualitative agreement. By contrast to the case of dripping, where the droplet breakup process occurs at a fixed location and depends on the capillary number Ca_T, droplet formation in jetting occurs at the tip of a convected jet and remains relatively independent of Ca_T. The influence of the capillary number on dripping λ is evident through their complex evolution when solely plotted as a function of φ in Figure 5c. While jetting droplet size scales as $d/h \sim \varphi^{1/3}$, the corresponding wavelength is found to scale analogous to theory in the absence of external flow, $\lambda/h \sim \varphi^{1/4}$. Overall, the wavelength is a useful parameter as it encompasses effects due to droplet deformation and droplet spacing and permits a comparison with other regimes, including wave regimes, which are incorporated in the graph and found at large φ and appear to have a lower boundary of $\lambda^*/h \sim 1$.

Ultimately, it is instructive to examine the morphology of dispersed flows having various aspect ratios d/L. In the dripping regime, combining individual scaling laws for d and L yields the simple estimate $d/L \sim \varphi$ where the individual influence of Ca_T on each variable is compensated. A simple argument based on mass conservation of one-dimensional segmented flows over a time period T also indicates that $dh^2 \sim TQ_1$ while $Lh^2 \sim TQ_2$, leading to $d/L \sim \varphi$ for large droplets. Here, the scaling $d/L = 3\varphi$ shows very good agreement with dripping droplets (Figure 5d). By contrast to the dripping regime, the aspect ratio d/L of jetting flows practically levels near the value of 0.5 at small φ and data are well fit with the expression $d/L = 0.5 + 3\varphi$.

3.3. Separated Flows. *3.3.1. Stable Jet Length.* In this section, we analyze viscous multiphase flows using an approach based on continuous streams. The time-averaged lateral width of the central stream provides a useful metric to compare the spatial evolution of dispersed and separated flows. As a central stream made of discrete droplets or having continuous periodic undulations delineates a steady envelope of amplitude A_E, we examine the longitudinal evolution of A_E to determine the jet development length L_S, corresponding to the distance between the injection needle of width b/h at $x = 0$ and the location where the amplitude remains constant, *i.e.*, $dA_E/dx = 0$, for various flow conditions.

In the tubing regime, we observe an abrupt broadening of A_E at the transition between the thin, wavy jet formed at the needle and the thick central core of the inner phase that occupies the full apparent cross section of the tube further downstream (Figure 6a). Other flow regimes, such as wave, jetting, and dripping, display a more gradual evolution of L_S (Figure 6b). In the case of the jetting regime of dispersed flows, the development length L_S coincides with the stable jet length before droplets are emitted from the tip of the jet. As a result, we adopt the terminology of stable jet length for L_S for all dispersed and separated flow regimes.

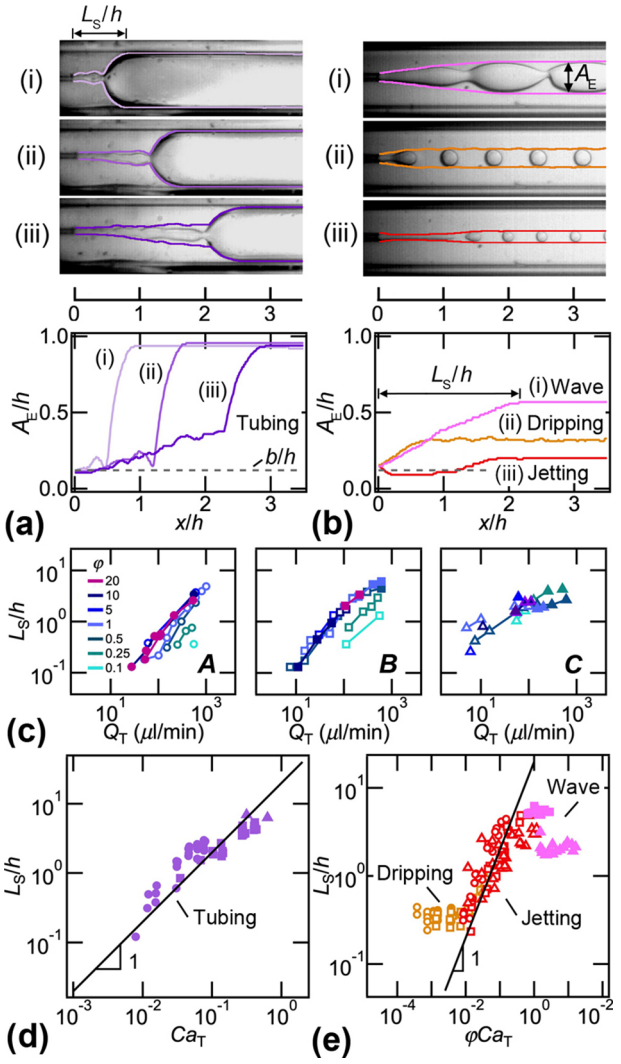

Figure 6. Stable jet length L_S in coaxial microchannels. (a) Examples of measurement of L_S from spatial evolution of envelope amplitude $A_E(x)$ in the tubing regime. Flow rates (Q_1, Q_2) in μL/min. Micrographs: Fluid pair A, (i) (50, 10), (ii) (75, 10), and (iii) (400, 10). (b) Measurement of L_S in wave, jetting, and dripping regimes. Micrographs: Fluid pair C, (i) (50, 10), (ii) (100, 10), and (iii) (200, 10). (c) Evolution of L_S/h along iso-φ curves as a function of Q_T for fluid pairs A, B, and C. Open symbols: Dispersed flows. Solid symbols: Separated flows. (d) Normalized jet length L_S/h *versus* Ca_T for the tubing pattern. Solid line: $L_S/h = 20Ca_T$. (e) Variations of L_S/h as a function of φCa_T for wave, jetting, and dripping regimes. Solid line: $L_S/h = 20\varphi Ca_T$.

Systematic measurements of L_S at fixed $\varphi = Q_1/Q_2$ are displayed as a function of $Q_T = Q_1 + Q_2$ for immiscible fluid pairs in Figure 6c. For each fluid pair, data points collapse on a single curve depending on Q_T at large $\varphi > 1$ and separate into various curves at low $\varphi < 1$, suggesting a dependency on both

https://doi.org/10.1021/acs.langmuir.1c00782
Langmuir 2021, 37, 7420−7429

φ and Q_T for diluted flows. To account for the influence of interfacial tension γ_{12} on the evolution of the stable length across fluid pairs, we plot L_S/h as a function of the capillary number Ca_T for the tubing regime and find good agreement with the simple scaling $L_S/h = 20Ca_T$ (Figure 6d). For other regimes at lower φ, the parameter φCa_T enables collapsing data points onto a single S-shaped curve, which remains mostly constant, $L_S/h \sim 0.5$ for dripping flows at low φCa_T, shows a quasi-linear growth for jetting flows, $L_S/h = 20\varphi Ca_T$, in an intermediate range, and a plateau $L_S/h \sim 5$ for wavy flows at large φCa_T (Figure 6e). Overall, the scaling relationship $L_S/h \sim \varphi Ca_T$ in the jetting regime at low $\varphi \ll 1$ suggests that the jet length primarily depends on Q_1 in the case of low viscosity contrast $\chi \ll 1$. By contrast, when the inner phase is highly viscous, other previous work showed a scaling of the form $L_S/h \sim (Q_1Q_2)^{1/2}$ in square microchannels.[22]

3.3.2. Jet Width and Film Thickness. Another feature of multiphase flows in parallel microchannels consists in the lateral extension of fully developed fluid streams, which strongly depend on fluid properties and flow conditions. The methodological acquisition of flow patterns based on systematic variations of flow rates of injection, Q_1 and Q_2, for fluids having constant $\chi = \eta_1/\eta_2 \sim 10^{-2}$ allows us to independently reveal the influence of interfacial tension γ_{12} and flow velocity Q_T/h^2 for flows having fixed φ. For instance, Figure 7a displays the evolution of flow patterns for $\varphi = 0.2$ for fluid pairs A to D with variations of Q_T over two orders of magnitude. This approach shows that at fixed Q_T, increasing γ_{12} widens the envelope amplitude A_E of the central stream, *i.e.*, produces larger droplets. By contrast, augmenting Q_T at fixed γ_{12} reduces the droplet size for immiscible fluids while for miscible fluids, the initial central stream width ε remains approximately constant.

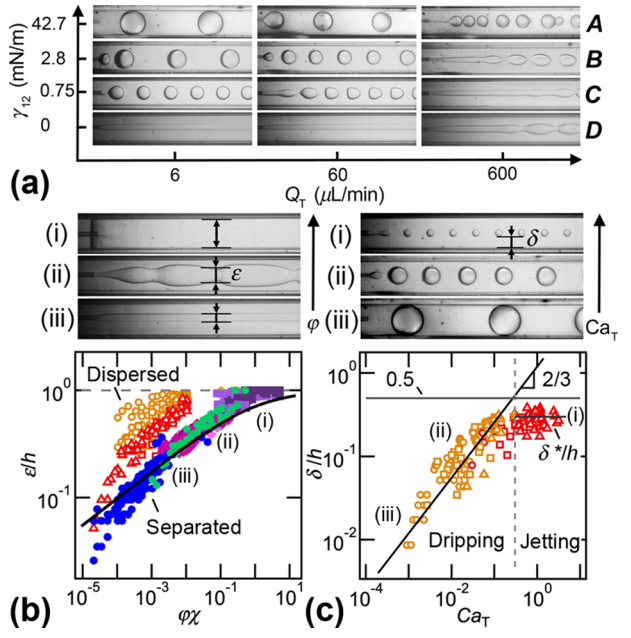

Figure 7. Evolution of average jet diameter ε and film thickness δ. Flow rates (Q_1, Q_2) in μL/min. (a) Chart of multiphase flow morphology at fixed $\varphi = Q_1/Q_2 = 0.2$ for fluid pairs A to D for various average flow rates $Q_T = Q_1 + Q_2 = 6$ with (1, 5), 60 with (10, 50), and 600 with (100, 500). (b) Top: Micrographs for (i) fluid pair C (75, 2.5) and (ii) (100, 10) and (iii) fluid pair D (7.5, 50). Bottom: Evolution of average jet diameter ε/h for separated flows [tubing (■), stable jet (●), diffusive jet (⬢), and waves (♦)] and envelope amplitude A_E for dispersed flows [dripping (○) and jetting (△)] as a function of $\chi\varphi$. Solid line: $\varepsilon/h = [1 + (\varphi\chi)^{-1/2}]^{-1/2}$ (c) Top: Micrographs for (i) fluid pair C (1, 50), (ii) fluid pair B (10, 50), and (iii) fluid pair A (1, 5). Bottom: Normalized film thickness δ/h *versus* Ca_T for immiscible fluid pairs. Solid line: $\delta/h = 1.2Ca_T^{2/3}$, $\delta^*/h = 0.3$.

In the stable jet regime, the normalized inner phase diameter ε/h is measured using image processing as the distance between two peaks of gray values in the intensity profile of a segment drawn normal to the flow direction. For low viscosity contrast $\chi \ll 1$ in circular capillaries, simple modeling for core-annular[34] flows shows $\varepsilon/h = [1 + (\varphi\chi)^{-1/2}]^{-1/2}$, which is found in good agreement with stable jet data as well as with those for other separated flow regimes in square channels (Figure 7b). In the diffuse jet regime, a similar profile analysis for ε/h is conducted downstream the stable jet length near the microneedle. For wave regimes, we measure ε/h as the average normalized amplitude of wave crests and troughs. Overall, the central stream diameter of separated flow depends on φ and remains independent of Q_T. A somewhat opposite trend is found for dispersed flows, where the envelope amplitude A_E strongly depends on Q_T and is independent of φ. When plotted against $\varphi\chi$ in Figure 7b, the envelope amplitude A_E of dispersed flows shows significantly larger values compared to ε/h of separated flows.

Measurements of A_E enable estimating the film thickness δ between walls and droplets according to $\delta = (h - A_E)/2$, which show good agreement with classic Bretherton scaling[40] where the relation $\delta/h = 1.2Ca_T^{2/3}$ is shown to curve-fit data for both dripping and jetting droplets at a low capillary number $Ca_T < 0.2$ (Figure 7c). At larger Ca_T, the film thickness δ/h appears to level around a value of 0.3 for $Ca_T \sim 1$. The overall trend for δ/h suggests that the film reaches the limiting value of 0.5 for $Ca_T \gg 1$ due to microchannel confinement.

3.3.3. Wavy Flows. An intriguing mode of deformation of separated flows resides in the development of periodic waves along the core of the central stream. We observe two main types of periodic waves, including capillary waves having relatively large wavelength of undulation λ with immiscible fluids and inertial waves with small λ for both miscible and immiscible fluids. In general, the wavelength of perturbations is seen to decrease with increasing Reynolds number $Re = \rho_1 Q_T/(\eta_1 h)$. For moderate $Re > 10$, however, the spatial period tends toward a minimal value $\lambda^*/h \sim 1$ (Figure 8a). Therefore, we plot $(\lambda/h - 1)$ as a function of Re and find a robust scaling $(\lambda/h - 1) = 8Re^{-2}$ (Figure 8a—inset). The exponent −2 for the Reynolds number is similar to previous work on the stability of core-annular flow in larger systems,[41] where a relation of the type $\lambda \sim 1/Re^2$ was observed. Here, the expression $\lambda/h = 1 + 8/Re^2$ permits an estimation of wave morphology based on external control parameters.

Another characteristic of interest is the wave frequency f, which can be measured from the average time period $T = 1/f$ between two wave crests using spatiotemporal diagrams made along lines drawn normal to the flow direction on high-speed movies (Figure 8b—inset). It is instructive to compare the wave frequency f to the average shear rate of the core V_i/h, where V_i is the interfacial velocity between the inner and outer stream. In turn, the interfacial velocity can be estimated as $V_i = 2(Q_2/h^2)$ for low viscosity contrasts $\chi \ll 1$ and direct proportionality is found between frequency and shear rate according to $f = aV_i/h$, with constant $a = 1.5$ (Figure 8b). Independent measurements and characterization of primary

https://doi.org/10.1021/acs.langmuir.1c00782
Langmuir 2021, 37, 7420−7429

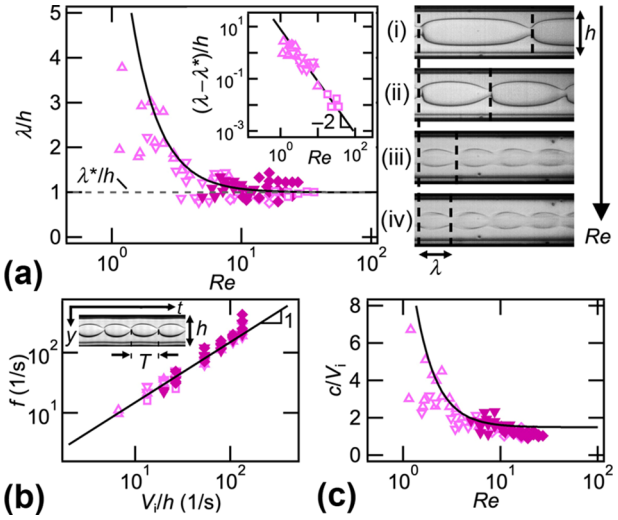

Figure 8. Capillary and inertial wave characteristics. (a) Normalized wavelength λ/h as a function of Reynolds number Re. Solid line: $\lambda/h = 1 + 8\mathrm{Re}^{-2}$. Inset: Scaling relationship between $(\lambda/h - 1)$ and Re. Solid line: $(\lambda/h - 1) = 8\mathrm{Re}^{-2}$. Flow rates ($Q_1$, Q_2) in μL/min. Micrographs: (i) Fluid pair C (100, 25) and (ii) (100, 50) and (iii) fluid pair E (100, 200) and (iv) (100, 300). (b) Wave frequency f *versus* interfacial shear rate V_i/h. Solid line: $f = 1.5\ V_i/h$. Inset: Example of spatiotemporal diagram showing a wave period T. (c) Normalized celerity c/V_i *versus* Re. Solid line: $c/V_i = 1.5(1 + 8\mathrm{Re}^{-2})$.

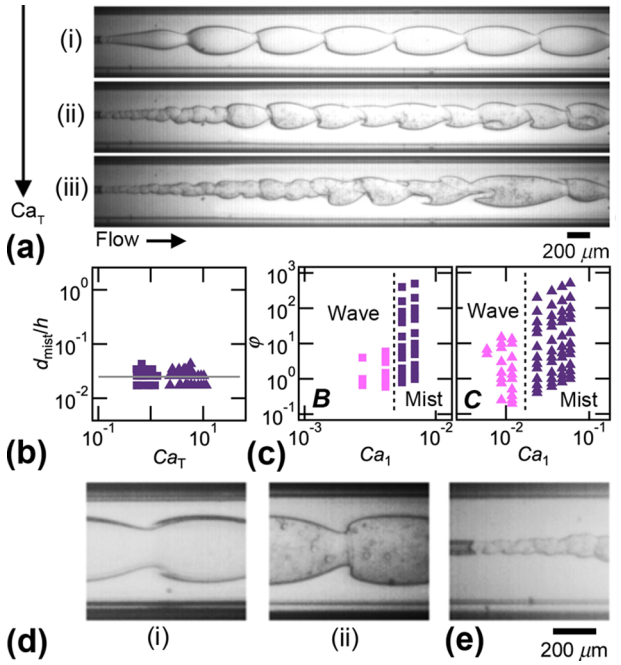

Figure 9. Wavy mist flow. (a) Micrographs showing the formation of mist flows for fixed $\varphi = 1$ at large Ca_T, fluid pair C, flow rates (Q_1, Q_2) in μL/min, (i) (100, 100), (ii) (300, 300), and (iii) (500, 500). (b) Average mist droplet diameter d_{mist}/h *versus* Ca_T. Solid line: $d_{mist}/h = 2.5 \times 10^{-2}$. (c) Transition from wavy to mist flows based on φ and Ca_1. Solid lines: $\mathrm{Ca}_1 = 4.8 \times 10^{-3}$ for fluid pair B and $\mathrm{Ca}_1 = 1.7 \times 10^{-2}$ for fluid pair C. (d) Detailed view of the wave crest for (300, 50) with (i) fluid pair D and (ii) fluid pair C. (e) Closeup view of rough initial jet corresponding to (a) (ii).

quantities λ and f are useful for predicting the wave celerity c using the basic wave equation according to $c = \lambda f = a(1 + 8\mathrm{Re}^{-2})V_i$. To probe this relationship, the celerity c is experimentally measured using high-speed imaging by recording the distance in which the wave crest travels during a certain duration. As can be seen in Figure 8c, data associated with measurements of normalized wave celerity c/V_i are satisfactorily fit with the expression $c/V_i = 1.5(1 + 8\mathrm{Re}^{-2})$, which shows that wave celerity tends to V_i at large flow velocity Q_T/h.

3.3.4. Mist Flows. Finally, we discuss the phenomenology of mist flows, which consist in the entrainment of minute droplets of the outer fluid L2 into the central stream made of fluid L1. These flows present features of both dispersed and separated flows and can be seen as a form of a partial phase inversion with respect to the device injection scheme. As droplets are initially formed along the interface of continuous streams, however, mist flows are characteristic of separated flows at large flow rates Q_T, such as tubing and wave regimes. For a given jet diameter ε/h, the concentration of mist droplets in the core stream increases with the flow rate, as can be seen in Figure 9a where $\varphi = Q_1/Q_2$ is fixed at unity and $Q_T = Q_1 + Q_2$ is varied for fluid pair C.

The size of mist droplets d_{mist}/h typically ranges between 10^{-2} and 10^{-1} with an average at 2.5×10^{-2} (Figure 9b). Therefore, mist droplets are significantly smaller than droplets emitted from entrained filaments at the crest of developed inertial waves with $\lambda/h \sim 1$. Such comparatively large ligament droplets typically develop further downstream and can be seen in Figure 9aii,iii. The gradual transition from capillary to mist waves is accompanied with a loss regularity of the wave pattern due to the progressive inclusion of high-viscosity material in the central core stream, which can lead to wave merging further downstream and an overall increase in the effective central stream diameter ε. In practice, we find that mist droplets appear in the central stream above a critical jet flow rate Q_1, which yields a critical inner phase capillary number $Ca_1 = \eta_1 Q_1/(\gamma_{12} h^2)$ for the transition of 4.8×10^{-3} for fluid pair B and of 1.7×10^{-2} for fluid pair C (Figure 9c).

While lowering interfacial tension γ_{12} favors the formation of mist droplets, such droplets are not observed for miscible fluids, as shown in Figure 9d, where under identical flow conditions, the central stream of the miscible fluid pair D remains clear of droplets while mist flows are observed for the immiscible fluid pair C. In the miscible case, ligaments form at wave crests and elongate along the channel before blending by diffusion. By contrast, in the immiscible case, wave crests are surrounded by tiny droplets, which create a mist in the inner phase. Overall, data show that mist droplets are generated during the initial jet deceleration from the microneedle into the main channel. Given our small centerline injector, $b/h \sim 10^{-1}$, the interfacial area of discharging jets appears significantly distorted with a miniature wave forming at large Q_1 (Figure 9e). In turn, capillary breakup of small ligaments entrained from miniature wave crests of diverging rough jets leads to the formation of droplet clouds made of a high-viscosity fluid. While beyond the scope of this study, our experimental data show the development of circular motion in the sheath fluid near the injection needle, which hints at the presence of a vortex ring near the central orifice at large φ and high Q_T. Hence, for a given fluid pair, mist droplets are formed as a result of the complex interplay between flow geometry and flow parameters and further work is required to fully characterize this intriguing regime.

https://doi.org/10.1021/acs.langmuir.1c00782
Langmuir 2021, 37, 7420−7429

4. CONCLUSIONS

This study provides an overview of the influence of interfacial tension γ_{12} on liquid−liquid multiphase flows having a large difference in viscosity in coaxial microchannels. To reveal the role of interfacial properties, a systematic series of experiments are conducted using fluid pairs having constant viscosity contrasts $\chi \sim 10^{-2}$ for both immiscible and miscible fluid pairs in identical microflow devices, characterized with a microneedle diameter $b/h \sim 10^{-1}$. We analyze the main features of some familiar and less familiar microflow regimes and methodically draw and compare flow maps over a wide range of injection flow rates Q_1 and Q_2. This approach enables refining criteria for regime definition and facilitates the development of scaling arguments for flow transitions. Specifically, we show the interplay between fluid properties and flow parameters and characterize the evolution of quantities across flow patterns. For dispersed flows, we discuss the evolution of primary parameters, such as droplet size d and spacing L, and examine the modification of compound parameters, such as wavelength $\lambda = d + L$ and aspect ratio d/L, in dripping and jetting flows. In the case of separated flows, we quantitatively compare flow patterns formed between immiscible fluid pairs and miscible fluids pairs, which serve as a control group to better delineate the influence of non-negligible interfacial tension on microflow morphology and dynamics. Basic core-annular flows provide a useful reference in the study of wave regimes, and measurements of quantities, such as the stable jet length and the envelope amplitude of both continuous and discrete streams, permit a unifying method for investigating viscous multiphase flow patterns over a wide range of interfacial tension γ_{12}. Our approach shows that for similar microgeometries and analogous flow conditions, a reduction in γ_{12} leads to a decrease in the droplet size d with implications on microflow arrangements of immiscible fluids. The asymptotic regime of core-annular flow is recovered when γ_{12} tends to nullity for miscible fluids, thereby unifying the phenomenological description of miscible and immiscible fluids flows in microfluidic channels.

We also uncover intriguing microflow regimes, including mist flows for immiscible fluids with ultralow γ_{12} and inverted thread flows for miscible fluids, in which the more-viscous liquid becomes encapsulated by the less-viscous liquid at large Q_T and high φ. Our work suggests that such flow patterns are characteristic of concentric microflow devices having a very small injection needle $b/h \ll 1$ and result from the complex hydrodynamic interplay at the transition between concentric flows and core-annular flows at the microneedle. Our results indeed indicate the presence of vortex rings developing in the concentric sheath flow near the needle due to a significant relative change in stream velocities. A better understanding of the formation and implication of vortex rings on multiphase in coaxial microchannels would provide new capabilities for improved manipulations of viscous and soft materials at the small scale. Future work could investigate the influence of the needle size b/h on a variety of viscosity-differing liquid multiphase flows in the presence and in the absence of a surfactant. Overall, the development of numerical and theoretical predictions would also help in elucidating the complex physicochemical hydrodynamics associated with coaxial microdevices. The microfluidic mist flow regime is of prime interest for finely emulsifying high-viscosity fluids at moderate Reynolds numbers and offers a new route for controlling the composition of multiphase materials.

AUTHOR INFORMATION

Corresponding Author

Thomas Cubaud − *Department of Mechanical Engineering, Stony Brook University, Stony Brook, New York 11794, United States;* orcid.org/0000-0002-9296-0783; Email: thomas.cubaud@stonybrook.edu

Author

Thai Dinh − *Department of Mechanical Engineering, Stony Brook University, Stony Brook, New York 11794, United States*

Complete contact information is available at: https://pubs.acs.org/10.1021/acs.langmuir.1c00782

Notes

The authors declare no competing financial interest.

ACKNOWLEDGMENTS

We have appreciated insightful discussions with Xiaoyi Hu.

REFERENCES

(1) Leal-Calderon, F.; Schmitt, V.; Bibette, J. *Emulsion Science: Basic Principles*; Springer: New York, 2007; p 5.

(2) Zinchenko, A. Z.; Davis, R. H. Motion of deformable drops through porous media. *Annu. Rev. Fluid. Mech.* **2017**, *49*, 71.

(3) Butt, H.-J.; Graf, K.; Kappl, M. *Physics and Chemistry of Interfaces*; Wiley-VCH: Weinheim, 2006; p 1.

(4) Thompson, D. A. W. *On Growth and Form: A New Edition*; Cambridge University Press: Cambridge, 1942; p 351.

(5) Joseph, D. D.; Renardy, Y. Y. *Fundamentals of Two-Fluid Dynamics. Part II: Lubricated Transport, Drops and Miscible Liquids*; Springer-Verlag: New York, 1993; p 326.

(6) Hu, X.; Cubaud, T. Viscous wave breaking and ligament formation in microfluidic systems. *Phys. Rev. Lett.* **2018**, *121*, 044502.

(7) Bolognesi, G.; Hargreaves, A.; Ward, A. D.; Kirby, A. K.; Bain, C. D.; Ces, O. Microfluidic generation of monodisperse ultra-low interfacial tension oil droplets in water. *RSC Adv.* **2015**, *5*, 8114.

(8) Moiré, M.; Peysson, Y.; Herzhaft, B.; Pannacci, N.; Gallaire, F.; Augello, L.; Dalmazzone, C.; Colin, A. Ultralow interfacial tension measurement through Jetting/Dripping Transition. *Langmuir* **2017**, *33*, 2531.

(9) Truzzolillo, D.; Cipelletti, L. Off-equilibrium surface tension in miscible fluids. *Soft Matter* **2017**, *13*, 13.

(10) Carbonaro, A.; Cipelletti, L.; Truzzolillo, D. Ultralow effective interfacial tension between miscible molecular fluids. *Phys. Rev. Fluids* **2020**, *5*, 074001.

(11) Brennen, C. E. *Fundamentals of Multiphase Flows*; Cambridge University Press: Cambridge, 2005; p 163.

(12) Umbanhowar, P. B.; Prasad, V.; Weitz, D. A. Monodisperse emulsion generation via drop break off in a coflowing stream. *Langmuir* **2000**, *16*, 347.

(13) Lorenceau, E.; Sang, Y. Y. C.; Höhler, R.; Cohen-Addad, S. A high rate flow-focusing foam generator. *Phys. Fluids* **2006**, *18*, 097103.

(14) Bremond, N.; Bibette, J. Exploring emulsion science with microfluidics. *Soft Matter* **2012**, *8*, 10549.

(15) Anna, S. L. Droplets and bubbles in microfluidic devices. *Annu. Rev. Fluid. Mech.* **2016**, *48*, 285.

(16) Doufène, K.; Tourné-Péteilh, C.; Etienne, P.; Aubert-Pouëssel, A. Microfluidic systems for droplet generation in aqueous continuous phases: A focus review. *Langmuir* **2019**, *35*, 12597.

(17) Montanero, J. M.; Gañán-Calvo, A. M. Dripping, jetting and tip streaming. *Rep. Prog. Phys.* **2020**, *83*, 097001.

(18) Garstecki, P.; Fuerstman, M. J.; Stone, H. A.; Whitesides, G. M. Formation of droplets and bubbles in a microfluidic T-junction-scaling and mechanism of break-up. *Lab Chip* **2006**, *6*, 437.
(19) Baroud, C. N.; Willaime, H. Multiphase flows in microfluidics. *C. R. Phys.* **2004**, *5*, 547.
(20) Baroud, C. N.; Gallaire, F.; Dangla, R. Dynamics of microfluidic droplets. *Lab Chip* **2010**, *10*, 2032.
(21) Seo, M.; Paquet, C.; Nie, Z.; Xu, S.; Kumacheva, E. Microfluidic consecutive flow-focusing droplet generators. *Soft Matter* **2007**, *3*, 986.
(22) Cubaud, T.; Mason, T. G. Capillary threads and viscous droplets in square microchannels. *Phys. Fluids* **2008**, *20*, 053302.
(23) Morin, B.; Liu, Y.; Alvarado, V.; Oakey, J. A microfluidic flow focusing platform to screen the evolution of crude oil-brine interfacial elasticity. *Lab Chip* **2016**, *16*, 3074.
(24) Chu, L.-Y.; Utada, A. S.; Shah, R. K.; Kim, J.-W.; Weitz, D. A. Controllable monodisperse multiple emulsions. *Angew. Chem., Int. Ed.* **2007**, *46*, 8970.
(25) Shah, R. K.; Shum, H. C.; Rowat, A. C.; Lee, D.; Agresti, J. J.; Utada, A. S.; Chu, L.-Y.; Kim, J.-W.; Fernandez-Nieves, A.; Martinez, C. J.; Weitz, D. A. Designer emulsions using microfluidics. *Mater. Today* **2008**, *11*, 18.
(26) Utada, A. S.; Fernandez-Nieves, A.; Stone, H. A.; Weitz, D. A. Dripping to jetting transitions in coflowing liquid streams. *Phys. Rev. Lett.* **2007**, *99*, 094502.
(27) Adams, L. L. A.; Kodger, T. E.; Kim, S.-H.; Shum, H. C.; Franke, T.; Weitz, D. A. Single step emulsification for the generation of multi-component double emulsions. *Soft Matter* **2012**, *8*, 10719.
(28) Jeong, W. J.; Kim, J. Y.; Choo, J.; Lee, E. K.; Han, C. S.; Beebe, D. J.; Seong, G. H.; Lee, S. H. Continuous fabrication of biocatalyst immobilized microparticles using photopolymerization and immiscible liquids in microfluidic systems. *Langmuir* **2005**, *21*, 3738.
(29) Hassan, A. A.; Sandre, O.; Cabuil, V.; Tabeling, P. Synthesis of iron oxide nanoparticles in a microfluidic device: preliminary results in a coaxial flow millichannel. *Chem. Commun.* **2008**, *15*, 1783.
(30) Shin, S.; Hong, J. S.; Lee, K.-H.; Lee, S.-H. Oil-Free Generation of Small Polymeric Particles Using a Coaxial Microfluidic Channel. *Langmuir* **2009**, *25*, 12361.
(31) Tottori, S.; Takeuchi, S. Formation of liquid rope coils in a coaxial microfluidic device. *RSC Adv.* **2015**, *5*, 33691.
(32) Hwang, C. M.; Khademhosseini, A.; Park, Y.; Sun, K.; Lee, S.-H. Microfluidic Chip-Based Fabrication of PLGA Microfiber Scaffolds for Tissue Engineering. *Langmuir* **2008**, *24*, 6845.
(33) Pullagura, B. K.; Gundabala, V. Microfluidics-based on-demand generation of nonwoven and single polymer microfibers. *Langmuir* **2020**, *36*, 1227.
(34) Hu, X.; Cubaud, T. From droplets to waves: periodic instability patterns in highly viscous microfluidic flows. *J. Fluid Mech.* **2020**, *887*, A27.
(35) Cubaud, T. Swelling of diffusive fluid threads in microchannels. *Phys. Rev. Lett.* **2020**, *125*, 174502.
(36) Hishida, K.; Maeda, M.; Ikai, S. Heat transfer from a flat plate in two-component mist flow. *J. Heat Transfer* **1980**, *102*, 513.
(37) Kumari, N.; Bahadur, V.; Hodes, M.; Salamon, T.; Kolodner, P.; Lyons, A.; Garimella, S. V. Analysis of evaporating mist flow for enhanced convective heat transfer. *Int. J. Heat Mass Transfer* **2010**, *53*, 3346.
(38) Lee, S. L.; Yang, Z. H.; Hsyua, Y. Cooling of a heated surface by mist flow. *J. Heat Transfer* **1994**, *116*, 167.
(39) Tomotika, S. On the instability of a cylindrical thread of a viscous liquid surrounded by another viscous fluid. *Proc. R. Soc. London, Ser. A* **1935**, *150*, 322.
(40) Bretherton, F. P. The motion of long bubbles in tubes. *J. Fluid Mech.* **1961**, *10*, 166.
(41) d'Ocle, M.; Martin, J.; Rakotomalala, N.; Salin, D.; Talon, L. Pear and mushroom instability patterns in two miscible fluids' core annular flows. *Phys. Fluids* **2008**, *20*, 024104.

https://doi.org/10.1021/acs.langmuir.1c00782
Langmuir 2021, 37, 7420−7429